Karl F. Warnick

Construction of an Inexpensive Anechoic Chamber and Its Applications in Undergraduate Research

Toan K. Vo Dai, Anh Thai, Tuan Phan, Ozlem Kilic, and Kevin Russo

Anechoic chambers provide isolated and controlled environments that minimize electromagnetic interference to enable measurements and testing of radio-frequency (RF) devices. Having access to such a facility enhances the learning experience of students as they undertake their first few electromagnetics courses. However, commercial anechoic chambers are expensive to acquire.

In this article, we provide a set of instructions that were used to construct a simple, cost-effective rectangular anechoic chamber for educational use at The Catholic University of America (CUA). We hope that future teams will find these instructions useful if they would like to fashion a similar chamber. This apparatus was built as part of a yearlong senior project and will be used by undergraduate and graduate students at CUA.

THE NEED FOR A HANDY APPARATUS

Anechoic chambers have been used for more than 60 years to create a free-space environment at microwave frequencies. The first anechoic chamber for antenna measurements appeared in 1953 and offered –20-dB reflection coefficients

EDITOR'S NOTE

Two articles are presented in this month's "Education Corner" column. In this first article, by Toan K. Vo Dai and colleagues at The Catholic University of America, an inexpensive radio-frequency test chamber for undergraduate research is described.

over 2.4–10 GHz. With the development of new-generation broadband absorbers that can offer better than –60-dB reflection coefficients for normal incidences at microwave frequencies, anechoic chambers began to play an important role in a variety of measurements requiring a highly effective quiet zone and low interference from the outside environment [1]–[4].

Anechoic chambers come in different shapes, such as rectangular, tapered, or dome shaped [1]–[7]. The vast majority are rectangular because of the simple design and construction involved. However, a disadvantage of such chambers is that they introduce unwanted scattering from the walls at low frequencies [5], [6]. While tapered chambers can overcome this issue, they are not suitable for measurements requiring multiple or moving sources because there is only a single-source antenna located at the taper's apex.

The chamber's accuracy was validated through return loss and insertion loss measurements. The results showed that

the constructed chamber performed well over a bandwidth of 8–40 GHz. Upon the successful manufacture of the chamber, two applications were investigated by undergraduate students to demonstrate the effectiveness of the chamber: 1) three-dimensional (3-D)-imaging of buried objects and 2) near-field antenna measurements.

ANECHOIC CHAMBER CONSTRUCTION

The anechoic chamber described in this article was designed and constructed as a cost-effective alternative for commercial products to give students at CUA access to experiments and measurements in their electromagnetics-related courses and research. The objective was to keep the chamber small and portable, so it could be carried around, and low in cost (US$2,500–US$3,000). The chamber is supported by a network analyzer. We chose a rectangular configuration because of its simple structure. The rectangular shape also allowed an easy arrangement of the absorbing materials.

As mentioned in the previous section, one crucial disadvantage of rectangular anechoic chambers at low frequencies (below 1 GHz) is the wide angles of reflection from the walls, ceiling, and floor. To address this issue, we designed our anechoic chamber to operate above 10 GHz. While we validated good performance over the 10–40-GHz bandwidth via our return loss and insertion loss measurements, we anticipate that the chamber will operate well beyond 40 GHz, as our absorber specifications indicate that there is typical reflectivity at a normal incidence of –50 dB up to 50 GHz. This high frequency range not only helps reduce the wide angles of reflection but also keeps the overall size of the anechoic chamber small, which eventually reduces the cost of construction. While our chamber meets the requirements of isolation to support a number of applications, it does not have the utilities of commercially available products, which typically cost orders of magnitude more and are not affordable for basic research or educational use.

SPECIFICATIONS AND COMPONENTS

As mentioned previously, the lowest frequency for the chamber to operate was set at 10 GHz. It is expected to work up to 50 GHz because of the broadband characteristics of the absorber materials we used. The key factors in the construction of the chamber were its structure, the probe for the measurements, the absorbers, and the aluminum shielding.

The antennas used for our measurements were 20-dB WR90 standard horn antennas. From the dimensions of the antenna and the operating frequency band, we calculated the overall external dimensions of the chamber as $36 \times 36 \times 36$ in^3 to satisfy the far-field requirements. To aid in the speed and ease of construction, we purchased a wooden crate from the U-line Company (model S-13373) [8].

One of the vital steps in the construction of the chamber was the absorber placement. We opted for C-RAM SFC 8 absorbers and corner blocks provided by Cuming Microwave Company [9], and we used Velcro to attach them to and completely cover the crate's internal walls. The dimensions of the C-RAM SFC 8 absorber were $3 \times 3 \times 8$ in^3 per pyramid, and there were 64 pyramids in each piece. The size of the C-RAM corner blocks could be adjusted to fit inside the wooden crate. Figure 1(a) shows the arrangement of the absorbers after they were attached to the crate walls. Figure 1(b) shows the computer-assisted design (CAD) for the corner arrangement using the corner block and pyramidal absorbers. After completely covering the walls without any gaps, the internal dimensions of the chamber were $20 \times 20 \times 35$ in^3.

In the constructed chamber, we used flat absorbers to cover its base so it would be easier to place the device under test inside the chamber's quiet zone. Although we did not build a shielded cover for the top of the apparatus, we used absorbers to cover the metal frames around the antenna located at the top to reduce any interference, as we show in the section "Assembled Anechoic Chamber with Antenna Scanner and Estimated Cost."

ANECHOIC CHAMBER RF CHARACTERIZATION AFTER SHIELDING

Shielding helps reduce electromagnetic interference entering the chamber from outside. The chamber was shielded by covering its side walls and floor with aluminum foil. The aluminum foil we used was from the R.A. Mayes Company [10], with a thickness of 0.0025 in. Its insertion loss per layer was greater than 80 dB at 10 GHz. While it would have been ideal to also construct a shielding cover on the top wall of the chamber, this would have complicated our construction structure because we were to place a scanner on the top, as will be discussed in the section "3-D Imaging of Buried Objects Using the Chamber."

To validate the efficiency of the absorbers and shielding layer over a broad bandwidth, we measured the insertion loss and return loss [11] between two antennas over the 8–12-GHz and 18–40-GHz bandwidths. Although the performance was not measured over the 12–18-GHz range because of a lack of available antennas, the measurements over the two bands indicate that an equally good performance would be achieved.

The insertion loss measurement was implemented using two standard horn antennas working at 8–12 GHz (WR90, 20-dB gain) connected to our performance network analyzer (PNA) (Agilent PNA-X N5247A). In this measurement, the receiver was placed in the center of the chamber while the transmitter was sited 35 in from the chamber's external wall. The antenna centers were aligned by making sure that the distances from the antenna centers to the edge of the chamber's side wall were identical. For vertical alignment, the antenna centers were placed 10 in from the ground. The slopes of the faces of the horns were
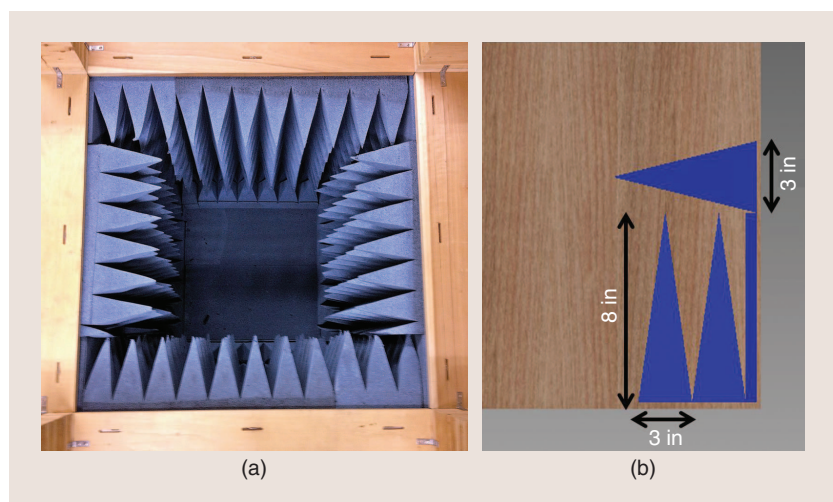

FIGURE 1. (a) The arrangement of the absorbers. (b) The CAD of the corner arrangement.

compensated for by raising the ends with a small absorber to vertically align the two antennas facing each other. The transmitter was connected to port 1 of the PNA to generate a 0-dBm signal.

Similarly, for the insertion loss measurement over the 18–40-GHz range, two 20-dB-gain horn antennas were used. Figure 2(a) shows that the insertion loss varies from –90 to –80 dBm over the 8–12-GHz range. For the return loss measurements, both the transmitter and receiver antennas were placed inside the chamber and pointed toward the same interior side wall. A thick piece of absorber was placed between them to prevent any coupling. As shown in Figure 2(b), the return loss

remained below –75 dBm for 8–12 GHz. These results were acceptable for our purposes and guaranteed that there would be no significant interference from outside or because of interior wall reflections. We note that the measured performance over the 18–40-GHz range was similar, with an average return loss of –80 dBm and an insertion loss of –85 dBm across the band. Because of space constraints, we show only the insertion loss and return loss performance for the 8–12-GHz range.

ANTENNA SCANNER CONSTRUCTION

An antenna scanner was built to sit on top of the chamber frame. Its functionality is to move an antenna looking toward

the apparatus's quiet zone to a desired location over a plane on top of the chamber. We had to consider two important factors in the scanner design: 1) precision in accurately positioning at a desired location and 2) tolerance to carry the weight of the antenna.

SPECIFICATIONS AND CONSTRUCTION

The overall dimensions of the scanner were chosen as 36×36 in^2 so that it could sit atop the chamber. The scanner was designed to completely cover the quiet zone region, which was designed as $20 \times 20 \times 35$ in^3. The estimated weight that the scanner had to be able to carry was about 20 lb, including the sliders, motors, and mounted antenna. The scanner was constructed using a supporting main frame as well as a Y-slider and an X-slider corresponding to the two orthogonal directions on the plane of the top surface.

SUPPORTING MAIN FRAME AND Y-SLIDER

Figure 3 shows the main frame constructed from 1×1-in^2 and 1×2-in^2 T-slots. These T-slots were fixed using 3/4-in angle brackets. The Y-slider was built using a 1×3-in^2 T-slot. The 1.5-in white nylon rollers were secured under the Y-slider for motion. The rollers were connected to the 2-in angle brackets, which formed a 45° angle with the frame to enhance the stability of the rollers and the Y-slider. Timing pulleys were then used to enable the motions of the Y-slider, with the help of stepper motors.

X-SLIDER

The X-slider was built and mounted on the Y-slider. It is used to carry different types of antennas with typical weights of about 2–4 lb. Figure 4 shows
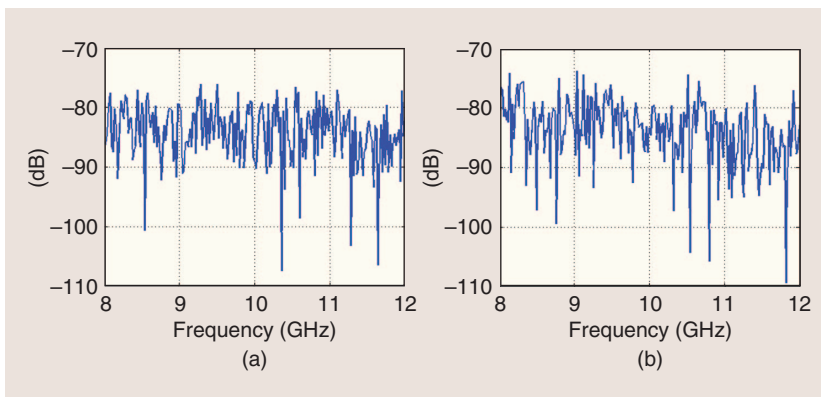

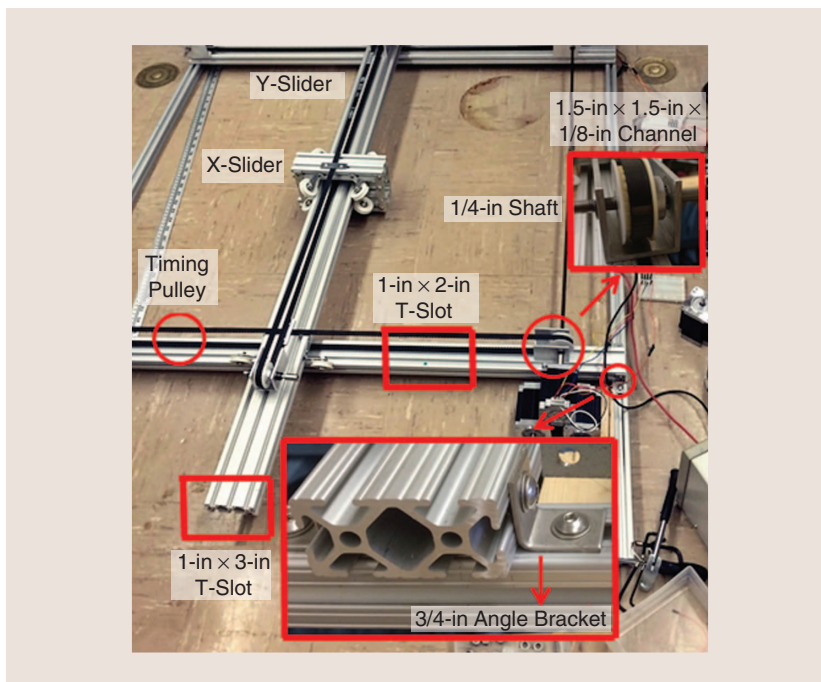FIGURE 2. (a) The insertion loss and (b) return loss over 8–12 GHz.

FIGURE 3. The construction of the main frame and Y-slider using T-slots.
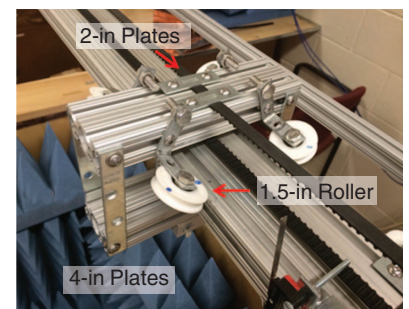

FIGURE 4. The X-slider after assembly.

the assembled X-slider, where stepper motors were mounted on the main frame of the scanner. Rollers and timing pulleys were connected to the X-slider in a manner similar to the Y-slider.

ABSORBERS TO COVER THE METAL FRAME

To simplify our structure design and cut costs, we did not have a shielded cover for the top of the chamber. As a result, unwanted reflected fields could be created due to the interactions among the objects under test, the antenna, and the metal frame of the antenna scanner. These unwanted reflected signals could affect the fields measured by the probe/antenna. To reduce the unwanted reflections from the frame of the antenna scanner or the probe and to improve the quality of the measurements, we placed absorbers along the Y-slider, as shown in Figure 5(a), and around the aperture of the probe used for measurements [Figure 5(b)]. Our measurements indicated a significant improvement when compared to results without these absorbers on the slider.

SOFTWARE AND CIRCUITRY OF THE ANTENNA SCANNER

An Arduino Mega 2560 [12] was used to control the motors, with the support of Big Easy Drivers. The inputs needed for the scanner's operation, such as the maximum length of the x and y axes (L_x, L_y) and the sampling step size on these axes $(\Delta x, \Delta y)$, are sent to the Arduino through a local area network protocol using an Arduino Ethernet Shield. Feedback is also provided from the Arduino to the user after each successive scanning location. One stepper motor was used for the X-slider, and two motors were used for the Y-slider because it has to carry the X-slider as well as the mounted antenna (a total weight of 20 lb). Therefore, using two synchronizing motors helps increase the stability and precision of the Y-slider. With the chosen stepper motors, the antenna scanner can carry up to 20 lb on the Y-slider and 10 lb on the X-slider.

The smallest step size our scanner can achieve is 0.3 in in both the x and y directions. The factor that limits the step size of the scanner is its weight. A smaller step size decreases the total torque the motors can carry and move the sliders. Limit switches were also used for safety; they were placed at both ends of the sliders and connected directly to the main power supply so they could automatically cut off the power in the event of a slider malfunction. Information about the antenna location on the rectangular grid was displayed through a liquid crystal display (LCD) to keep track of the scanner's operation. Figure 6 shows the schematic of the circuitry used to control the scanner.

ASSEMBLED ANECHOIC CHAMBER WITH ANTENNA SCANNER AND ESTIMATED COST

The assembled chamber with the antenna scanner sitting on top is shown in Figure 7. The chamber is supported by our network analyzer. Data from the network analyzer are sent directly to the computer through the Virtual Instrument Standard Architecture (VISA), which is a standard defined by Agilent Technologies and National Instruments for communicating with instruments regardless of the interface. Communication was established through a VISA instrument object, which we created in MATLAB.

Table 1 specifies the itemized cost of the required components and their quantities to construct the chamber and the antenna scanner. The total cost for the construction was approximately US$2,700.

3-D IMAGING OF BURIED OBJECTS USING THE CHAMBER

The main objective of 3-D imaging of objects buried in an unknown medium is to locate their position and reconstruct their shape. With recent improvements in both algorithm and hardware technologies, 3-D imaging of buried objects can be used in a variety of applications, such as land mine detection [13]–[20], bridge inspection [21]–[23], and road condition surveys [24], [25]. Standard back-projection algorithms have proven effective in such applications [26]–[30]. In this article, we present the results of our experiments by implementing measurements using the stepped-frequency approach

and then applying the standard back-projection algorithm to the stepped-frequency imaging.

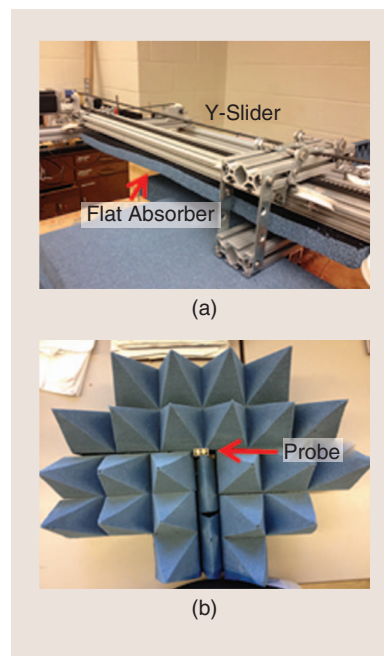As an electromagnetic signal penetrates a lossy medium, it slows down and

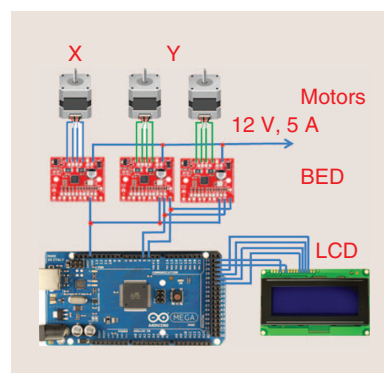**FIGURE 5.** The absorber covering (a) the top metal frame and (b) the probe to reduce interference.

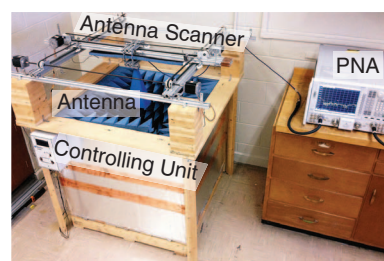**FIGURE 6.** The schematic for the controlling circuit. BED: big easy driver.

FIGURE 7. The assembled anechoic chamber and antenna scanner.

TABLE 1. THE COST ESTIMATES FOR ANECHOIC CHAMBER AND ANTENNA SCANNER CONSTRUCTION.

Categories	Main Items	Quantity	Total Expense (US$)
Chamber structure	Wooden crate, $36 \times 36 \times 36$ in^3	1	180
	C-RAM SFC 8 absorbers, $24 \times 24 \times 8$ in^3	15	900
	C-RAM corner blocks	6	200
	Aluminum foil, 0.0025-in thick	1	375
	Copper tape, 3-in width	1	150
Antenna scanner	T-slots, $1 \times 1 \times 72$ in^3	2	60
	T-slots, $1 \times 2 \times 72$ in^3	2	110
	T-slot, $1 \times 3 \times 72$ in^3	1	59
	3/4-in angle brackets	8	8
	2-in angle brackets	12	12
	1.5-in nylon rollers	12	72
	Trapezoidal tooth neoprene timing belts, 0.2-in pitch, 77-in outer circle, 3/8-in wide	3	45
	Acetal pulleys for XL-series	6	48
	Timing belts for 1/4-in and 3/8-in belt width	3	15
	$1.5 \times 1.5 \times 1/8$-in^3-thick channel aluminum	1	13
	1/4-in shaft collars	12	12
	1/4-in shafts	3	15
	2-in mending plates	6	12
	4-in mending plates	4	16
	10-32 3/8-in stainless screws (hex head)	100	5
	10-32 7/16-in stainless screws (hex head)	100	7
	10-32 3/8-in square nuts	50	10
	10-32 3/8-in washers	50	8
	10-32 3/8-in split lock washers	100	8
	1/4-20 3/4-in hex head cap screws	50	5
Controller circuitry	Arduino Mega 2560	1	46
	Arduino Ethernet Shield	1	45
	NEMA 23 stepper motors, 200 steps/revolution, 57 mm $\times$ 76 mm, 8.6 V, 1 A/phase	3	150
	Big Easy Drivers	3	60
	Limit switches	4	12
	LCD, 20×4	1	13
	ac to dc adapter, 12 V, 5 A	1	20
	TOTAL		**2,691**

becomes attenuated. In addition, its path is deformed, a result that depends on the relative permittivity and conductivity of the medium. All of these effects must be compensated for to acquire a buried object's reconstructed image. Although a set of exact equations can be used to analyze the medium's effect on the propagation delay based on Snell's law in [31], this method can be complicated because it requires numerically solving numerous transcendental equations.

A simpler method, which approximates the medium's effect, was proposed in [32] based on the propagation delay minimization method. In this article, we apply the concept in [32] to account for the effect of the medium on the imaging results. An overview of the notion of the back-projection imaging approach in free space is introduced in the next section. We then employ our time-minimization technique for objects buried in sand.

IMAGING ALGORITHM FOR DETECTING BURIED OBJECTS AND THE TIME-MINIMIZATION METHOD

Consider a plane with $M \times N$ samples located at $z = 0$. The object resides at position (x_p, y_p, z_p) inside a sandbox, which is placed in the quiet zone of the chamber, as shown in Figure 8. Assume that a wideband signal $s(t)$ is sent from the antenna at location $(m, n, 0)$. If the reflection coefficient of the target in Figure 8 is Γ, then the received signal at the antenna is

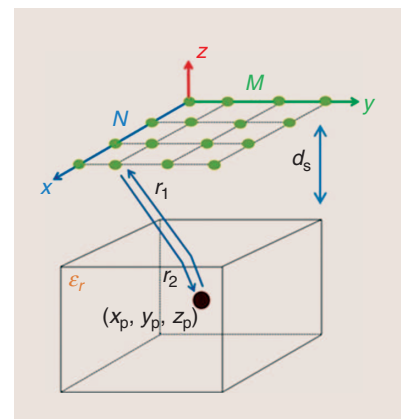$$E_s(m, n, t) = \Gamma \cdot s(t - t_{\text{travel}}), \quad (1)$$

FIGURE 8. An imaging model for a buried object.

with the propagation delay $t_{\text{travel}} = (r_1/c) + (r_2/v) = (r_1 + \sqrt{\varepsilon_r} r_2/c)$, where r_1 and r_2 are the propagation paths in air and in the medium, respectively, c is the speed of light, and ε_r is the relative permittivity of the medium.

The idea of the standard back-projection algorithm [30] is represented in (2), where matched filtering is first applied to the scattered field received at each antenna location. By summing the matched-filter response results from all of the antenna locations, the intensity of a pixel (x, y, z) can be calculated as

$$f(x, y, z) = \iiint w(m, n) E_s(m, n, t) \times \delta(t - t_{\text{travel}}) dt \, dm \, dn, \quad (2)$$

where $f(x, y, z)$ is the intensity at each pixel in the imaging regions, $w(m, n)$ is the weighting function on the scan positions based on the radiation pattern of the scan antenna, and $E_s(m, n, t)$ is the scattered field received at antenna location $(m, n, 0)$.

Using the expression in [32], we can calculate r_1 and r_2 as

$$r_1 = \sqrt{d_s^2 + (x_s - m)^2 + (y_s - n)^2}, \quad (3)$$

$$r_2 = \sqrt{(z_p + d_s)^2 (x_s - x_p)^2 (y_s - y_p)^2}, \quad (4)$$

where d_s is the distance from the antenna plane to the interface of the medium, x_s and y_s denote the coordinates of the sampling points on the air–medium interface, and $x_p, y_p,$ and z_p are the coordinates of the pixel in the imaging region. There are two unknowns in (3) and (4): x_s and y_s. To identify their values, we recall the physical principle that when the wave propagates from point $(m, n, 0)$ to point (x_p, y_p, z_p), it will always choose a unique path such that the propagation delay is minimized, resulting in a refracted path. Therefore, the propagation delay for the model in Figure 8 can be described as

$$t_{\text{travel}} = \min_{x_s, y_s} \left(\frac{r_1}{c} + \frac{\sqrt{\varepsilon_r} r_2}{c} \right). \quad (5)$$

By substituting this value for t_{travel} obtained from (5) in (2), we can calculate the intensity of each pixel in the image of the buried object.
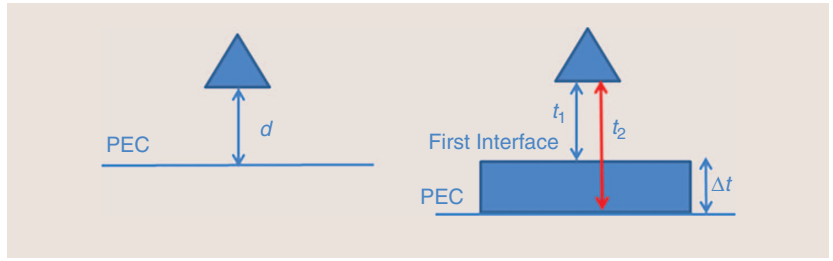

FIGURE 9. The measurement procedure for dielectric constant estimation.

ESTIMATION OF THE DIELECTRIC CONSTANT (ε_r) OF THE MEDIUM

The accurate estimation of the dielectric constant of the medium plays a crucial role in the accuracy of the generated images. There are various methods for the estimation of the media parameters [33]–[35]. For this article, we employed the time-domain reflectometry (TDR) proposed in [35]. The measurement can be carried out from one side of the medium and does not require any positioning system. The main goal of this method is to estimate the reflection coefficient at the first interface of the medium and use Fresnel's equation to calculate the dielectric constant. We can write the reflection coefficient as a function of the permittivity of the two interacting media as

$$\Gamma = \frac{\sqrt{\varepsilon_a} - \sqrt{\varepsilon_r}}{\sqrt{\varepsilon_a} + \sqrt{\varepsilon_r}}, \quad (6)$$

where, in this case, $\varepsilon_a = 1$ is the permittivity of air. Then, the unknown dielectric value can be calculated as

$$\varepsilon_r = \frac{(1 - \Gamma)^2}{(1 + \Gamma)^2}. \quad (7)$$

To find the reflection coefficient of the first interface of the medium, we need to use a perfect electrical conductor (PEC) ($\Gamma = -1$) to measure the time-domain response of the PEC as a reference measurement, denoted by $p(t)$, because, in practice, we do not know the characteristics of the incident wave. Afterward, the response from the actual medium [denoted by $w(t)$] is measured. The reflection coefficient at the surface of the medium is then estimated as

$$\Gamma = \frac{\|w(t)\|_\infty}{\|p(t)\|_\infty} \Gamma_{\text{PEC}} = -\frac{\|w(t)\|_\infty}{\|p(t)\|_\infty}. \quad (8)$$

From the measured reflection coefficient in (8), we calculate the relative

permittivity ε_r of the medium using (7). We can thus estimate the velocity in the medium as well as the thickness of the medium as follows:

$$v_s = \frac{c}{\sqrt{\varepsilon_r}}, \quad (9)$$

$$d_s = \frac{v \Delta t}{2}, \quad (10)$$

where Δt is the propagation time within the medium. With this method, Δt can be calculated by taking the difference between the time position of the second and first maxima of $w(t)$, which refer to the reflection of the bottom and top layer of the medium, as shown in Figure 9. To keep the measurement procedure simple, a PEC surface was placed under the medium so that we could keep track of the scattered signal from the first interface of the medium and from the aluminum panel in the back.

To validate this approach, we placed a 3.5-in-thick plastic box filled with dry sand inside the quiet zone of the chamber. The box was backed with a PEC layer made of aluminum. The top layer of the sand was 40 in away from the antenna aperture. We employed a stepped-frequency continuous wave (SFCW) signal spanning 8–12 GHz. The step between the two adjacent frequencies was chosen as 20 MHz. Figure 10 shows the time
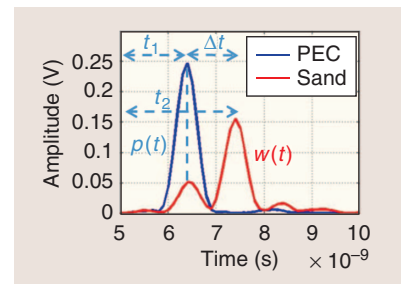

FIGURE 10. The time-domain response of dry soil layer.

response due to the referenced PEC and the soil layers.

Employing the TDR method, we first estimated the dielectric value of the sand and then used this estimated value to compute the thickness of the sandbox. As observed in the results shown in Table 2, we were able to estimate the dielectric constant within a 7% error margin. Our estimation of the permittivity of dry sand at 10 GHz was well within the published range, which indicates $\varepsilon_r = 2.5$ in [36].

MEASUREMENT RESULTS FOR DETECTING BURIED OBJECTS

Five different objects were created for measurements using aluminum foil (the letters C, U, and A) and copper tape (a square and a circular plate), as shown in Figure 11(a). We employed an SFCW signal with a bandwidth of 4 GHz at the center frequency of 10 GHz. The step between the two adjacent frequencies was chosen as 20 MHz. The sandbox containing the buried objects was placed in the center of the quiet zone, its top surface 40 in from the antenna aperture, as shown in Figure 11(b). The spacing between the grid points of the antenna positions was set at 0.6 in in both the x and y directions.

Figures 12 and 13 show planar slices of the buried objects at a depth of 1.5 in from the top surface of the sand using the back-projection algorithm based on the time-minimization method. The white line in each case depicts the actual object shape. A permittivity of 2.32 was assumed for the sand, as measured in the previous setup.

As we can observe in Figures 12 and 13, the image results replicated the objects well. The quality of images also depended on how the objects were buried inside the sand. For instance, if the surface of an object was perfectly parallel with the antenna aperture, the resulting image was detected well. However, if it was not parallel to the antenna aperture, the results were worse, as can be seen in the case of the letter A in Figure 13.

MEASUREMENT SENSITIVITY

In this section, we discuss some important issues that affect our imaging results.

ANTENNA SPACING AND RESOLUTION

The range resolution depends on the velocity v of the wave inside the medium and the bandwidth B of the SFCW, as described in (11) and (12). We denote the theoretical resolution in the z direction as ΔR_z, and we take it that

$$\Delta R_z = \frac{v}{2B}. \qquad (11)$$

The cross-range resolutions are approximately calculated [19], [28] as

$$\Delta R_{x,y} = \frac{R\lambda}{2D_{SA}}, \qquad (12)$$

where R is the distance from the antenna aperture to the surface of the medium, λ is the center operational wavelength, and D_{SA} is the length of the synthetic array formed by moving a single antenna along a straight path. In this measurement, we operated at a center frequency of 10 GHz, and the object under test was 40 in away. We employed a synthetic aperture of 20×20 in^2. Therefore, our cross-range resolution was $\Delta R_{x,y} \sim 1.2$ in. To verify the theoretical range resolution, we implemented two measurements by placing two square plates with dimensions of 4.7 in and 3.5 in at center-to-center separations of 0.4 in and 1.6 in. The first case
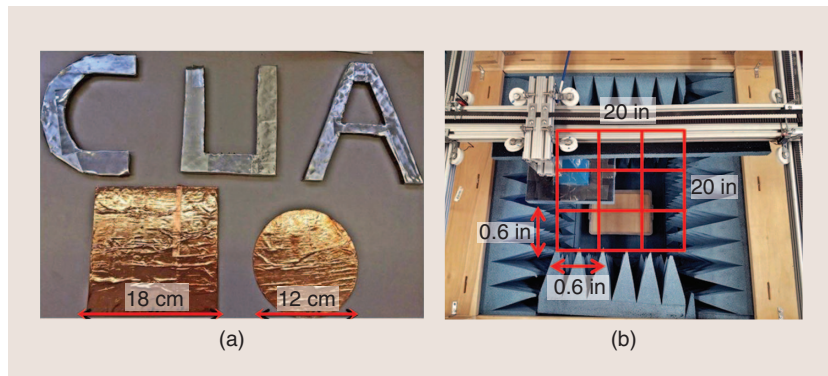
TABLE 2. THE ESTIMATION OF THE PERMITTIVITY AND THICKNESS OF THE SAND.			
Materials	**Estimated Value**	**Actual Value**	**Error (%)**
Permittivity (ε_r)	2.32	2.5	7
Thickness (in)	3.7	3.5	5

FIGURE 11. (a) The objects used in the measurements. (b) The measurement setup for a buried object.
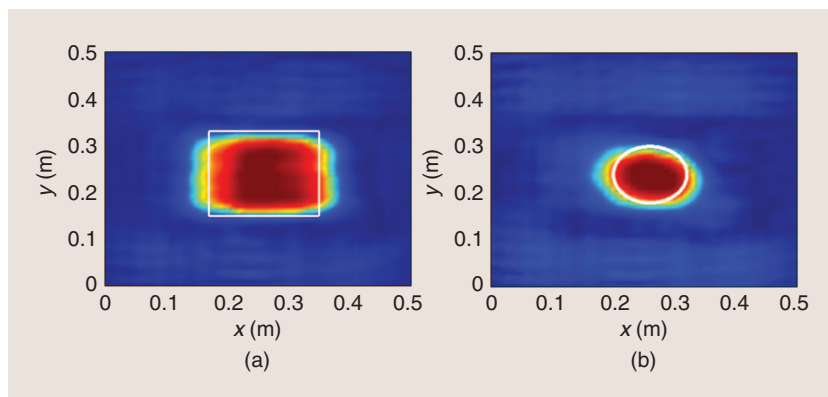

FIGURE 12. A planar slice at 1.5 in from the top with (a) the square plate and (b) the circular plate.
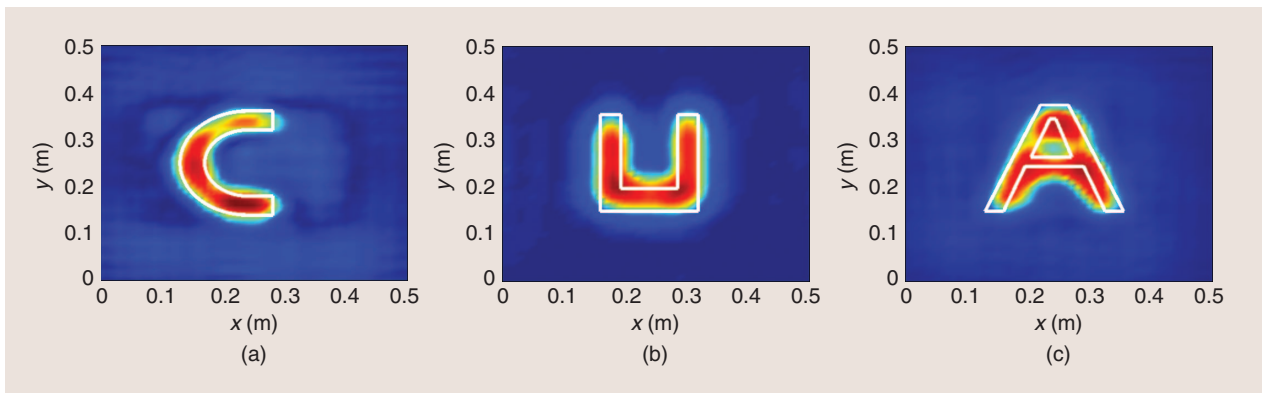
FIGURE 13. A planar slice at 1.5 in from the top with letters (a) C, (b) U, and (c) A.

corresponded to a scenario where the separation was smaller than our resolution, while the latter had a separation larger than our resolution limit. Because of the resolution limitation, we could not clearly distinguish the two objects with a 0.4-in separation [Figure 14(a)]. However, we could resolve them when they were separated by 1.6 in [Figure 14(b)].

BACKGROUND SUBTRACTION

Numerous mechanisms contribute to the signals received at each antenna position in this measurement, such as the scattered fields from the object under test, the scattered signal from the surface of the medium the object is buried in, and the reflection signal from the PEC panel at the bottom of the medium container. These scattered fields may result in unwanted artifacts in the image if they are not removed prior to signal processing through a background subtraction process. The background subtraction can be performed by applying the time-gating filter to the received signal. The range profile from a 7-in square plate and the corresponding sliced images with and without gating are shown in Figures 15 and 16, respectively. Without the background subtraction, the reconstructed image of the object is significantly distorted.

NEAR-FIELD ANTENNA MEASUREMENTS USING THE CHAMBER

The far-field characteristics of antennas are important in many electromagnetics applications. Measurements of far-field antenna patterns can be difficult in
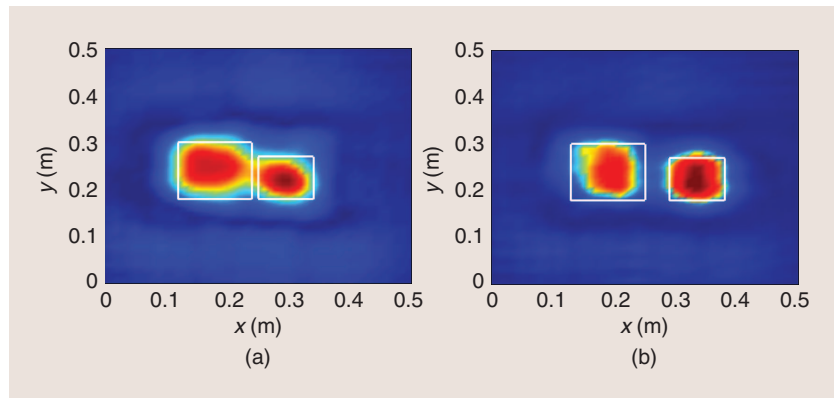

FIGURE 14. The effects of cross-range resolution: two square plates with (a) a 0.4-in separation and (b) a 1.6-in separation.
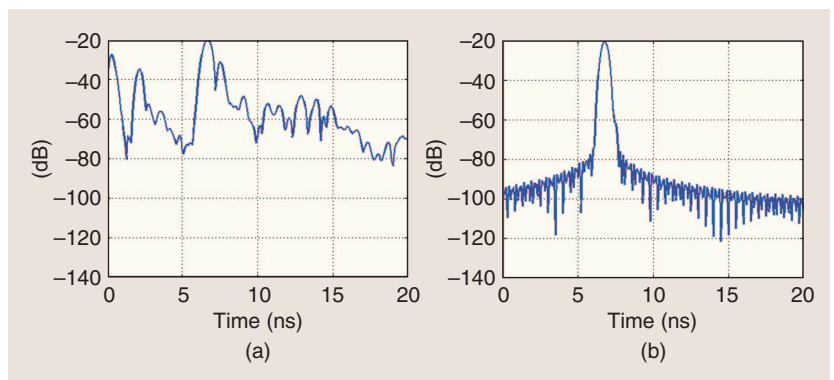

FIGURE 15. The range profile (a) without gating and (b) with gating.

practice because they require anechoic chambers with large dimensions. Therefore, it is sometimes convenient to measure the near-field characteristics of an antenna and then use analytical methods to calculate its far-field radiation patterns [37]–[42]. This can be achieved by using the near-field to far-field (NF/FF) transformation algorithm. Near-field components can be measured over a selected surface, which can be planar, cylindrical,

or spherical. The measured data allow the calculation of the field at any distance from the antenna using the principle of the modal expansion method.

MODAL EXPANSION ALGORITHM FOR PLANAR SYSTEMS

The mathematical formulations of the NF/FF systems are established on the basis of plane wave expansion using Fourier transform techniques [37]. It is stated
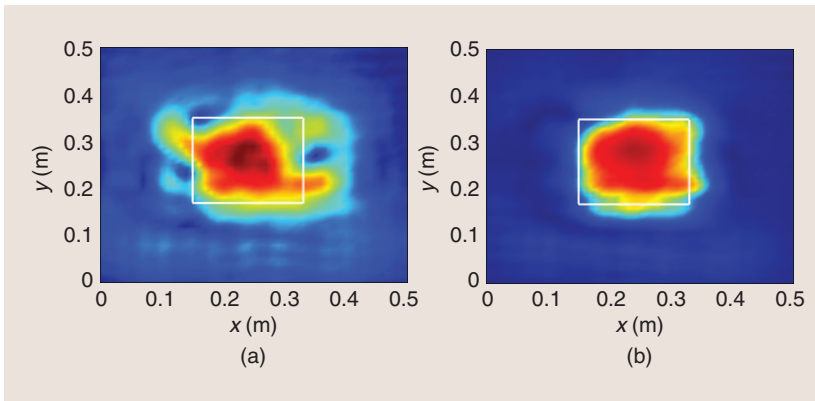
FIGURE 16. A planar slice of the 7-in square plate at a depth of 1.6 in from the top (a) without gating and (b) with gating.
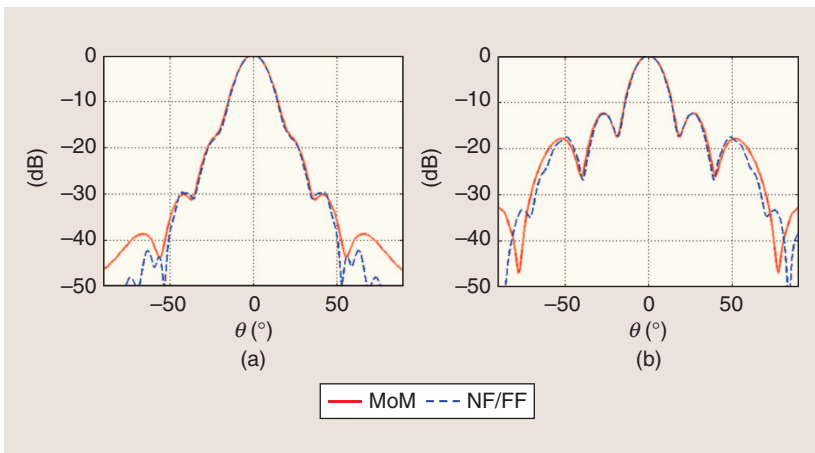

FIGURE 17. The far-field pattern in (a) the E-plane and (b) the H-plane, comparing the use of MoM and a simulation using NF/FF.

that any arbitrary wave at a given frequency can be represented as a superposition of plane waves traveling in different directions with different magnitudes. The relationship between the near-field E-field measurements and the far field for a planar system is as follows:

$$f_x(k_x, k_y) = \int_{-b/2}^{b/2} \int_{-a/2}^{a/2} E_{xa}(x, y, z = 0)$$
$$\times e^{j(k_x x + k_y y)} dx dy, \quad (13)$$

$$f_y(k_x, k_y) = \int_{-b/2}^{b/2} \int_{-a/2}^{a/2} E_{ya}(x, y, z = 0)$$
$$\times e^{j(k_x x + k_y y)} dx dy, \quad (14)$$

$$E_\theta(r, \theta, \phi) = j \frac{k e^{-jkr}}{2\pi r} (f_x \cos\phi + f_y \sin\phi), \quad (15)$$

$$E_\phi(r, \theta, \phi) = j \frac{k e^{-jkr}}{2\pi r} (f_y \cos\phi + f_x \sin\phi), \quad (16)$$

where E_{xa}, E_{ya} are the measured field components at the measurement plane

and $f_x(k_x, k_y)$ and $f_y(k_x, k_y)$ are the x and y components of the plane wave spectrum, which are determined in terms of the near-electric-field components. E_θ and E_ϕ are the far-field components we want to calculate. These equations are used assuming ideal probes. Thus, for accurate transformation to far-field radiation patterns, we need to correct for the receiving response of the probe. This process is called *probe correction* [43]–[46].

SIMULATION AND RESULTS USING A NONIDEAL PROBE

For this article, we measured the characteristics of a standard WR90 horn antenna (dimensions: 3.7×4.7 in^2 and length 11.05 in) with a half-power beamwidth of 16° and a gain of 20 dB. To model and validate the modal expansion method, the commercial

software package FEKO was used to simulate the horn antenna. We first obtained the near-field components from the model and then applied the modal expansion method to calculate the far-field radiation pattern of this horn antenna. We also directly calculated the far-field characteristics of the same horn using method of moments (MoM) in FEKO.

Because a measurement with an ideal probe is not practical, we implemented the simulation using an open-ended waveguide. Its advantage is that it minimizes the effect of a probe's radiation pattern on the measurement results while using a more directive antenna, as a probe might introduce errors due to its narrow beamwidth. We chose an open-ended waveguide with dimensions of $0.9 \times 0.4 \times 3.1$ in^3, corresponding to a half-power beamwidth of 122° on the E-plane and 64° on the H-plane. In the simulation, the probe was placed at the $z = 0$ plane, and the antenna under test (AUT) was 3.5 in away. A sampling step of 0.4 in was used in both directions.

Figure 17 compares the far-field results in both the E- and H-planes obtained directly from MoM with those obtained from our NF/FF transformation algorithm. As observed, a close match was achieved.

MEASUREMENT SETUP AND RESULTS

The near-field measurement of the antenna was implemented using the same parameters as in the simulation procedure discussed earlier. The scanning region dimensions were 20×20 in^2. The AUT was placed inside the chamber 3.5 in away from the open-ended waveguide. The AUT was connected to port 1 of the PNA-X 5247 A as the transmitter, while the probe was connected to port 2 as the receiver. A total of 47×47 data points were collected, corresponding to a sampling step of 0.4 in in both the x and y directions.

Figure 18 compares the measured far-field results using our chamber and the NF/FF transformation algorithm with the far-field calculations of the
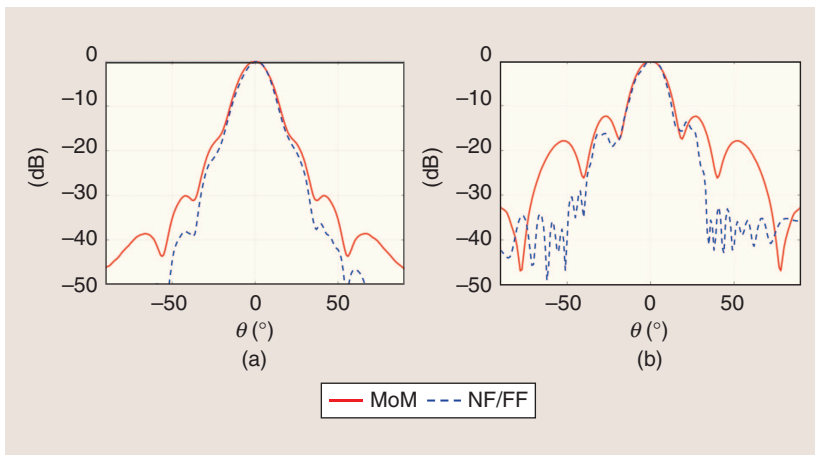
FIGURE 18. The far-field pattern in (a) the E-plane and (b) the H-plane, comparing the use of MoM and the measured NF/FF.

AUT using MoM in FEKO. The solid red line denotes the full-wave simulations—hence, the exact far-field pattern for the AUT. The dashed blue line corresponds to the NF/FF measurements. We observe a good match up to about −30 dB.

CONCLUSIONS

In this project, we built a low-cost anechoic chamber and antenna scanner, with total cost amounting to lower than US$3,000. The two were constructed as part of a senior design project and will be applied in the future to support the teaching of electromagnetics-related courses. As part of the project, two applications were implemented using the chamber: 1) 3-D imaging of buried objects and 2) near-field antenna measurement.

AUTHOR INFORMATION

Toan K. Vo Dai (30vodai@cua.edu) is a Ph.D. degree student and graduate research assistant in the Department of Electrical Engineering and Computer Science, The Catholic University of America, Washington, D.C. His research interests include bioinspired optimization methods, antenna design, and satellite communications systems.

Anh Thai (15thai@cua.edu) is an M.Sc. degree student in the Department of Electrical Engineering and Computer Science, The Catholic University of America, Washington, D.C. Her research interests include advanced imaging methods and high-performing computing.

Tuan Phan (30phan@cua.edu) is a Ph.D. degree student and teaching assistant in the Department of Electrical Engineering and Computer Science, The Catholic University of America, Washington, D.C. His research interests include numerical electromagnetics and high-performing computing.

Ozlem Kilic (kilic@cua.edu) is an associate professor in the Department of Electrical Engineering and Computer Science, The Catholic University of America, Washington, D.C. Her research interests include antennas, wave propagation, satellite communications systems, and microwave remote sensing. She is a fellow of the Applied Computational Electromagnetics Society.

Kevin Russo (russok@cua.edu) is a senior engineer with the Naval Research Laboratory, Washington, D.C., and an adjunct faculty member in the Department of Electrical Engineering and Computer Science, The Catholic University of America, Washington, D.C. His research interests include antenna and microwave circuit design.

REFERENCES

[1] H. E. William, "Electromagnetic wave absorbers and anechoic chambers through the years," *IEEE Trans. Antennas Propag.*, vol. 21, no. 4, pp. 484–490, 1973.

[2] V. Rodriguez, "An open-boundary quad-ridged guide horn antenna for use as a source in antenna pattern measurement anechoic chambers," *IEEE Antennas Propag. Mag.*, vol. 48, no. 2, pp. 157–160, 2006.

[3] B. K. Chung, H. T. Chuah, and J. W. Bredow, "A microwave anechoic chamber for radar-cross section measurement," *IEEE Antennas Propag. Mag.*, vol. 39, no. 3, pp. 21–26, 1997.

[4] C. L. Holloway, R. R. Delyser, R. F. German, P. McKenna, and M. Kanda, "Comparison of electromagnetic absorber used in anechoic and semi-anechoic chambers for emissions and immunity testing of digital devices," *IEEE Trans. Electromagn. Compat.*, vol. 39, no. 1, pp. 33–47, 1997.

[5] B. K. Chung and H. T. Chuah, "Design and construction of a multipurpose wideband anechoic chamber," *IEEE Antennas Propag. Mag.*, vol. 45, no. 6, pp. 41–47, 2003.

[6] M. R. Gillette, "RF anechoic chamber design using ray tracing," in *Proc. IEEE Antennas and Propagation Society Int. Symp.*, 1977, pp. 246–249.

[7] A. K. Fung, "Remote sensing at the University of Texas at Arlington," *IEEE Geosci. Remote Sens. Soc. Newslett.*, pp. 23–27, 1994.

[8] U-line Company. (2016). About us. [Online]. Available: https://www.uline.com/Corporate/About_History.aspx

[9] Cuming Microwave Corporation. (2016). About us. [Online]. Available: https://www.cumingmicrowave.com

[10] R. A. Mayes Company, Inc. (2018). Products. [Online]. Available: http://www.ramayes.com/

[11] G. Garner, J. Wilkerson, M. M. Skeen, D. F. Patrick, R. D. Hodges, R. D. Schimizzi, S. R. Vora, Z. Feng, K. G. Gard, and M. B. Steer, "Acoustic-RF anechoic chamber construction and evaluation," in *Proc. IEEE Radio and Wireless Symp.*, 2008, pp. 331–334.

[12] Arduino. (2018). What is Arduino? [Online]. Available: https://www.arduino.cc/

[13] T. G. Savelyev, L. V. Kempen, H. Sahli, J. Sachs, and M. Sato, "Investigation of time-frequency features for GPR landmine discrimination," *IEEE Trans. Geosci. Remote Sens.*, vol. 45, no. 1, pp. 118–129, Jan. 2007.

[14] P. A. Torrione, C. S. Throckmorton, and L. M. Collins, "Performance of an adaptive feature-based processor for a wideband ground penetrating radar system," *IEEE Trans. Aerosp. Electron. Syst.*, vol. 42, no. 2, pp. 644–658, Apr. 2006.

[15] A. Sullivan, R. Damarla, N. Geng, Y. Dong, and L. Carin, "Ultrawideband synthetic aperture radar for detection of unexploded ordance: Modeling and measurements," *IEEE Trans. Antennas Propag.*, vol. 48, no. 9, pp. 1306–1315, Sept. 2000.

[16] P. Gader, M. Mystkowski, and Y. Zhao, "Landmine detection with ground penetrating radar using hidden Markov models," *IEEE Trans. Geosci. Remote Sens.*, vol. 39, no. 6, pp. 1131–1144, June 2001.

[17] M. E Johansson and J. E. Mast, "Three-dimensional ground-penetrating radar imaging using synthetic aperture time-domain focusing," in *Proc. Int. Society for Optics and Photonics*, vol. 2275, 1994, pp. 205–214.

[18] C. Cafforio, C. Pratti, and F. Rocca, "SAR data focusing using seismic migration techniques," *IEEE Trans. Aerosp. Electron. Syst.*, vol. 27, no. 2, pp. 194–207, Mar. 1991.

[19] L. Borcea, G. Papanicolaou, and H. Zhao, "Theory and applications of time reversal and interferometry imaging," *Inverse Problems*, vol. 19, no. 6, pp. S134–S164, Dec. 2003.

[20] S. Oh, "Iterative space-time domain fast multi resolution SAR imaging algorithms," Ph.D. dissertation, Georgia Inst. Technol., Atlanta, GA, Nov. 2001.

[21] Z. W. Wang, M. Zhou, G. G. Slabaugh, J. Zhai, and T. Fang, "Automatic detection of bridge deck condition from ground penetrating radar images," *IEEE Trans. Autom. Sci. Eng.*, vol. 8, no. 3, pp. 633–640, 2011.

[22] R. Parrillo, R. Roger, and A. Haggan, "Bridge deck condition assessment using ground penetrating radar," in *Proc. European Conf. Nondestructive Testing (ECNDT)*, Berlin, 2526, 2006, pp. 112–123.

[23] A. Simi, G. Manacorda, and A. Benedetto, "Bridge deck survey with high resolution ground penetrating radar," in *Proc. IEEE 14th Int. Conf. Ground Penetrating Radar*, 2012, pp. 489–495.

[24] Y. Xia, F. Yang, X. Qiao, and X. Xu, "Ground penetrating radar system applied in the underground concealed object detection," in *Proc. IEEE 15th Int. Conf. Ground Penetrating Radar*, 2014, pp. 811–814.

[25] A. Benedetto, F. Tosti, G. Schettini, and C. Twizere, "Evaluation of geotechnical stability of road using GPR," in *Proc. IEEE 6th Int. Workshop Advanced Ground Penetrating Radar*, 2011, pp. 1–6.

[26] J. E. Mast and E. M. Johansson, "Three-dimensional ground-penetrating radar imaging using multifrequency diffraction tomography," in *Proc. Int. Society for Optics and Photonics*, 1994. pp. 196–204.

[27] M. Rofheart and J. McCorkle, "Order $N^2\log(N)$ backprojector algorithm for focusing wide-angle wide bandwidth arbitrary-motion synthetic aperture radar," in *Proc. SPIE RadarSensor Technology*, vol. 2747, June 1996, pp. 25–36.

[28] T. Counts, A. C. Gurbuz, W. R. Scott, J. H. McClellan, and K. Kim, "Multistatic ground-penetrating radar experiments," *IEEE Trans. Geosci. Remote Sens.*, vol. 45, no. 8, pp. 2544–2553, 2007.

[29] M. Duman and A. C. Gurbuz, "3D imaging for ground-penetrating radars via dictionary dimension reduction," *Turkish J. Elect. Eng. Comput. Sci.*, vol. 23, no. 5, pp. 1242–1256, 2015.

[30] B. Panzner, A. Jöstingmeier, and A. Omar, "Radar signatures of complex buried objects in ground penetrating radar," *Int. J. Electron. Telecommun.*, vol. 57, no. 1, pp. 9–14, 2011.

[31] F. Ahmad, M. G. Amin, and S. A. Kassam, "Synthetic aperture beamformer for imaging through a dielectric wall," *IEEE Trans. Aerosp. Electron. Syst.*, vol. 41, no. 1, pp. 271–283, 2005.

[32] G. Cui, L. Kong, and J. Yang, "A back-projection algorithm to stepped-frequency synthetic aperture through-the-wall radar imaging," in *Proc. IEEE 1st Asian and Pacific Conf. Synthetic Aperture Radar*, 2007. doi: 10.1109/APSAR.2007.4418570.

[33] A. H. Muqaibel and A. Safaai-Jazi, "A new formulation for characterization of materials based on measured insertion transfer function," *IEEE Trans. Microw. Theory Techn.*, vol. 51, no. 8, pp. 1946–1951, 2003.

[34] A. Muqaibel, A. Safaai-Jazi, A. Bayram, A. M. Attiya, and S. M. Riad, "Ultrawideband through-the-wall propagation," *IEE Proc.: Microw., Antennas Propag.*, vol. 152, no. 6, pp. 581–588, 2005.

[35] M. Aftanas, J. Sachs, M. Drutarovsky, and D. Kocur, "Efficient and fast method of wall parameter estimation by using UWB radar system," *Frequenz*, vol. 63, no. 11–12, pp. 231–235, 2009.

[36] A. von Hippel, *Dielectric Materials and Applications*. Cambridge, MA: MIT Press, 1954.

[37] C. A. Balanis, *Antenna Theory: Analysis and Design*. Hoboken, NJ: Wiley, 2012.

[38] A. D. Yaghjian, "An overview of near-field antenna measurements," *IEEE Trans. Antennas Propag.*, vol. 34, no. 1, pp. 30–45, 1986.

[39] K. Persson and M. Gustafsson, "Reconstruction of equivalent currents using a near-field data transformation-with radome applications," *Progress Electromagn. Res.*, vol. 54, pp. 179–198, 2005. doi:10.2528/PIER04111602.

[40] C. F. Stubenrauch and A. C. Newell, "Some recent near-field antenna measurements at NBS," *Microw. J.*, vol. 23, pp. 37–42, Nov. 1980.

[41] J. Lemanczyk and F. H. Larsen, "Comparison of near-field range results," *IEEE Trans. Antennas Propag.*, vol. 36, no. 6, pp. 845–851, June 1988.

[42] J. J. Lee, E. M. Ferren, D. P. Woollen, and K. M. Lee, "Near-field probe used as a diagnostic tool to locate defective elements in an array antenna," *IEEE Trans. Antennas Propag.*, vol. 36, no. 6, pp. 884–889, June 1988.

[43] C. H. Schmidt, M. M. Leibfritz, and T. F. Eibert, "Fully probe-corrected near-field far-field transformation employing plane wave expansion and diagonal translation operators," *IEEE Trans. Antennas Propag.*, vol. 56, no. 3, pp. 737–746, 2008.

[44] D. T. Paris, W. Marshall Leach, and E. B. Joy, "Basic theory of probe-compensated near-field measurements," *IEEE Trans. Antennas Propag.*, vol. 26, no. 3, pp. 373–379, 1978.

[45] E. Joy and G. Rodrigue, "Applications of probe-compensated near-field measurements," *IEEE Trans. Antennas Propag.*, vol. 26, no. 3, pp. 379–389, 1978.

[46] P. Petre and T. K. Sarkar, "Differences between modal expansion and integral equation methods for planar near-field to far-field transformation," *Progress Electromagn. Res.*, vol. 12, pp. 37–56, 1996.

Teaching and Learning Electromagnetic Polarization Using Mobile Devices

Eng Leong Tan and Ding Yu Heh

The wide availability of smart handheld and mobile devices has provided educators with another opportunity to aid the teaching of electromagnetics (EM) courses with touch-based interactivity, allowing seamless teaching and learning. This article

EDITOR'S NOTE

Two articles are presented in this issue's "Education Corner" column. In this second article, the authors present a mobile device application that helps students learn the principles of electromagnetic polarization. The EMpolarization application is available for Apple devices.

explores how mobile devices may be used to enhance students' grasp of EM polarization concepts through a

special app designed to provide interactive visualization. It also helps instructors to effectively illustrate many wave